Energy Engineering

Tech Science Press

Doi:10.32604/ee.2025.073862

ARTICLE

Identification and Analysis of Aerodynamic Sound Sources in Wind Turbines Based on the Integration of Time-Domain De-Doppler and Orthogonal Matching Pursuit Techniques

Peng Wang[1,2], Zhiying Gao[1,2,*], Yongyan Chen[1], Rina Su[1,2], Yefei Bai[2], Jianlong Ma[1,2] and Tianhao Zhang[1]

[1]College of Energy and Power Engineering, Inner Mongolia University of Technology, Hohhot, 010051, China
[2]Key Laboratory of Wind Energy and Solar Energy Utilization Technology of Ministry of Education, Inner Mongolia University of Technology, Hohhot, 010051, China

*Corresponding Author: Zhiying Gao. Email: hawkwarm@imut.edu.cn

Received: 27 September 2025; Accepted: 22 December 2025; Published: 27 May 2026

ABSTRACT: We propose a novel procedure, Time-Domain De-Dopplerized Orthogonal Matching Pursuit deconvolution approach for the mapping of acoustic sources (TD-OMP-DAMAS), for separating aerodynamic noise sources distributed across wind turbine blades (WTB), a task that is typically hindered by mutual interference and spatial mixing. The proposed procedure is a two-stage, hybrid de-Doppler/sparse-reconstruction algorithm based on time-domain de-Doppler (TD, Stage 1) and an orthogonal matching pursuit (OMP)-based deconvolution scheme (Stage 2), enabling sparse-reconstruction techniques to be effectively applied in rotating-source scenarios. The method is validated using both simulated rotating-source data and wind-tunnel measurements, and its performance is systematically compared with several conventional approaches, including conventional beamforming (CBF), time-domain de-Doppler beamforming (TD-BF), and time-domain de-Doppler deconvolution approach for the mapping of acoustic sources (TD-DAMAS). Numerical results demonstrate that TD-OMP-DAMAS achieves the smallest localization error and the highest spatial resolution among all tested algorithms, while also maintaining strong robustness under low signal-to-noise ratio conditions and requiring significantly fewer iterations than TD-DAMAS to accurately converge to the true source positions. Wind-tunnel tests further show that, under an inflow velocity of 6 m/s and a tip-speed ratio of 4.5, the method improves spatial resolution by approximately 89% compared with CBF, confirming its superior capability in separating aerodynamic sources located on different WTB.

KEYWORDS: Wind turbine noise; source identification; DAMAS; orthogonal matching pursuit

1 Introduction

In the realm of renewable energy development, wind power generation has gained extensive application on account of its merits, including cleanliness and sustainability [1]. Nevertheless, during the operational phase of WTB, noise is emitted externally. This not only disrupts the surrounding living environment but also has the potential to exert adverse effects on the structural integrity and power output of wind turbines [2]. Consequently, the identification and localization of wind turbine noise have evolved into a crucial area of research.

In wind turbine noise localization, microphone arrays combined with sound source localization algorithms have become a widely adopted approach [3]. However, conventional beamforming (CBF) lacks an

accurate source model and therefore often produces distorted acoustic images, leading to inaccurate localization and misleading source distributions [4,5]. To address the resolution limitations of CBF, researchers have introduced deconvolution-based techniques such as DAMAS [6] and CLEAN-Source Coherence (CLEAN-SC) [7]. These methods aim to suppress sidelobe interference and enable the identification of distributed sources generated by rotating blades, even at frequencies below the Rayleigh limit. DAMAS improves source identification by reshaping the array point-spread function and stabilizing the beamforming output. However, it amplifies high-frequency noise and may generate spurious sources. Its computational cost also increases rapidly with the number of focal points, making it impractical for large grids [8]. DAMAS2 mitigates high-frequency artifacts through a Gaussian low-pass filter but still exhibits slow convergence in complex sound fields [9]. CLEAN-SC offers higher spatial resolution than CBF but often produces overly discrete source maps, reducing its ability to represent continuous noise distributions. To overcome this limitation, Arcondoulis et al. [10] integrated array pattern matching with CLEAN-SC and successfully identified trailing-edge noise on a NACA0012 airfoil while suppressing sidelobes. Nevertheless, this approach requires two independent acoustic measurements, increasing implementation complexity, and does not resolve the long runtimes associated with DAMAS-type algorithms. To improve computational efficiency, Padois and Berry [11] introduced Orthogonal Matching Pursuit (OMP) into acoustic deconvolution, significantly reducing the cost of DAMAS and enabling its application to large focal grids. Sarradj [12] further combined OMP with non-negative matrix factorization to address the sub-optimality of classical matching-pursuit methods and enhance deconvolution performance. However, OMP becomes less reliable under low signal-to-noise ratios (SNR), and Ning et al. [13] therefore coupled OMP with singular value decomposition (SVD) to suppress noise and achieve accurate localization of aircraft landing-gear sources in complex turbulent flows. Although OMP significantly accelerates the deconvolution process, it does not apply well to wind turbine noise. The aerodynamic sources move with the rotating blades, and the Doppler effect continuously shifts their apparent radiation centers. Consequently, CBF maps exhibit curved spatial tracks rather than isolated focal points. These trajectory-like patterns fundamentally conflict with the sparse point-source model assumed by OMP, resulting in unstable reconstruction and substantial localization errors.

Beyond the challenges of sidelobe interference and slow convergence, wind turbine noise localization is further complicated by the Doppler effect. Because the sources rotate with the blades, the received signals experience Doppler-induced frequency and amplitude modulation, making accurate identification even more difficult [14]. To address this issue, Sijtsma et al. [15] proposed the Rotating Source Identification (ROSI) method, which incorporates moving-source transfer functions and shear-layer corrections. ROSI successfully identifies broadband blade-tip sources in helicopter hovering conditions, whereas traditional methods can only reveal a blurred annular region. However, ROSI still suffers from insufficient spatial resolution at mid- and low frequencies. To improve angular discrimination, Zhang et al. [16] developed a segmented ROSI method, enabling the successful identification of azimuthal source variations in industrial fan noise. Ye and Li [17] further combined ROSI with CLEAN-SC, leveraging the high-resolution capability of CLEAN-SC to overcome the low-frequency resolution deficit of ROSI. Nevertheless, this hybrid method requires roughly twice the computational time of the original ROSI, reducing its practical efficiency. In addition, ROSI is a nonlinear inversion technique and does not satisfy the linear superposition assumption, making it incompatible with deconvolution algorithms. In contrast, the time-domain de-Doppler beamforming (TD-BF) method performs linear time resampling and delay correction on microphone signals, thereby preserving the linear convolution model and allowing direct integration with deconvolution techniques. TD-BF also requires only a single resampling operation based on the rotational speed, which helps reduce computational cost. However, like traditional beamforming, TD-BF exhibits wide sidelobes at mid and low frequencies. As

a result, sidelobes may be erroneously interpreted as actual sources, while true aerodynamic sources may be masked—posing significant challenges for wind turbine noise identification.

Building on the above analysis of existing research, this study proposes a TD-OMP-DAMAS Method that integrates TD processing with sparse reconstruction. The method addresses the current gap wherein existing sparse-reconstruction-based deconvolution techniques cannot be effectively applied to rotating sound-source scenarios. By overcoming Doppler-induced trajectory distortion, the proposed approach enables fast and accurate separation and localization of aerodynamic noise generated by wind turbine blades. The main contributions of this work are summarized as follows:

1. A sparse deconvolution framework for rotating-source scenarios is established. We are developing an OMP-DAMAS sparse reconstruction framework tailored for Doppler-affected rotating sources. This framework preserves high spatial resolution while substantially reducing computational time, thereby improving the overall efficiency and practicality of sound-source identification under rotational motion.
2. OMP-DAMAS is introduced to aerodynamic noise identification for wind turbines for the first time. This work represents the first application of OMP-DAMAS to wind-turbine aerodynamic noise. Through comprehensive simulations and wind-tunnel measurements, we demonstrate that the proposed TD-OMP-DAMAS method achieves accurate localization and effective source separation in complex rotating-source environments, validating both its effectiveness and engineering applicability.

The structure of this paper is arranged as follows: Section 2 elaborates on the theoretical model and implementation process of the proposed method; Section 3 evaluates the positioning performance of the algorithm by simulating a rotating sound source; Section 4 conducts wind tunnel experiments to verify and analyze the practical application effect of the method; Section 5 summarizes the work of the entire paper and looks forward to future research directions.

2 Background Theory

2.1 The Forward Propagation Model of Stationary Sound Sources and the CBF Methodology

The sound pressure measured by the microphone can be considered as the superposition of the sound fields of multiple sound sources [18]. Thus, in the forward propagation model of the stationary sound source depicted in Fig. 1, the sound field information $p(\boldsymbol{r}_m, t)$ resulting from the superposition of N monopole sound sources received by microphone $\boldsymbol{r}_m$ can be expressed as

$$p(\boldsymbol{r}_m, t) = \sum_{n=1}^{N} \frac{1}{4\pi \|\boldsymbol{r}_m - \boldsymbol{r}_n\|} s_n\left(t - \frac{\|\boldsymbol{r}_m - \boldsymbol{r}_n\|}{c}\right), \tag{1}$$

where $\boldsymbol{r}_m$ represents the spatial position at microphone m; t denotes the receiving time instant; c is the speed of sound; $\|\boldsymbol{r}_m - \boldsymbol{r}_n\|$ represents the distance form the sound source $\boldsymbol{r}_n$ to the microphone $\boldsymbol{r}_m$; and $s_n\left(t - \frac{\|\boldsymbol{r}_m - \boldsymbol{r}_n\|}{c}\right)$ represents the sound pressure signal of the sound source $\boldsymbol{r}_n$ at the moment $t - \frac{\|\boldsymbol{r}_m - \boldsymbol{r}_n\|}{c}$; $t \in [0, 1, 2 \ldots (L-1)]/F_s$ is represents the reception time of the microphone, L is the number of sampling points, and F_s are the sampling frequency.

The time-domain sound pressure signal of the sound source can be converted to the frequency—domain representation by virtue of the Fourier transform, which is given by

$$s_n(t) = \frac{1}{2\pi} \int_{-\infty}^{\infty} \hat{s}_n(\omega) \, \mathrm{e}^{-\mathrm{j}\omega t} d\omega, \tag{2}$$

where $\hat{s}_n(\omega)$ represents the frequency-domain signal corresponding to $s_n(t)$. Thus, the frequency-domain signal of microphone m can be obtained as

$$\hat{p}_m(\omega) = \sum_{n=1}^{N} \frac{1}{4\pi \boldsymbol{r}_{m,n}} \hat{s}_n(\omega) e^{-j\omega \boldsymbol{r}_{m,n}/c}, \tag{3}$$

where $\boldsymbol{r}_{m,n}$ represents the vector distance between the microphone $\boldsymbol{r}_m$ and the sound source $\boldsymbol{r}_n$.

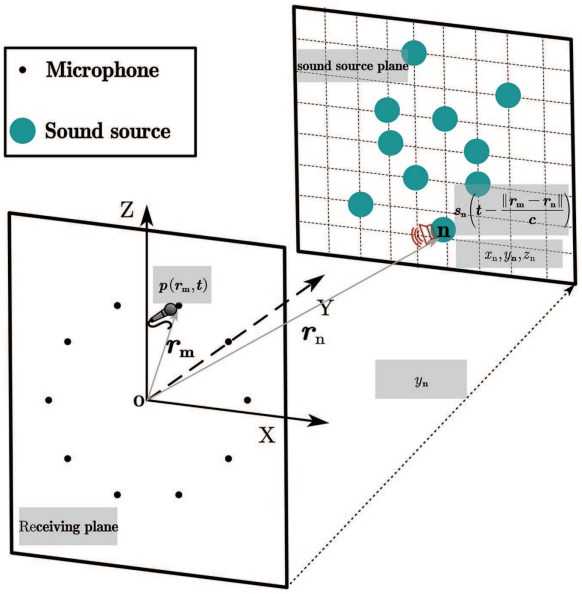

Figure 1: A schematic diagram of the acoustic pressure signal received by the microphone m at time t when it is at a distance of y_n from the sound source plane, radiated by sound source n

Assuming that the sound array has a total of M microphone channels, the entire array plane's frequency-domain sound field $\boldsymbol{P}(\omega)$ can be expressed as

$$\boldsymbol{P}(\omega) = \begin{bmatrix} \hat{p}_1(\omega) \\ \vdots \\ \hat{p}_M(\omega) \end{bmatrix} = \boldsymbol{G}(\omega)\boldsymbol{S}(\omega) + \boldsymbol{\eta}(\omega) = \begin{bmatrix} \frac{1}{4\pi r_{1,1}} e^{-j\omega r_{1,1}/c} & \cdots & \frac{1}{4\pi r_{1,N}} e^{-j\omega r_{1,N}c} \\ \vdots & \ddots & \vdots \\ \frac{1}{4\pi r_{M,1}} e^{-j\omega r_{M,1}/c} & \cdots & \frac{1}{4\pi r_{M,N}} e^{-j\omega r_{M,N}c} \end{bmatrix} \begin{bmatrix} \hat{s}_1(\omega) \\ \vdots \\ \hat{s}_N(\omega) \end{bmatrix} + \begin{bmatrix} \hat{\eta}_1(\omega) \\ \vdots \\ \hat{\eta}_M(\omega) \end{bmatrix}, \tag{4}$$

where, $\boldsymbol{G}(\omega)$ represents the matrix form of the frequency-domain Green's function, which is the transfer function for calculating the acoustic field response; $\boldsymbol{S}(\omega)$ represents the frequency-domain matrix of the sound source signal; and $\boldsymbol{\eta}(\omega)$ represents the microphone self-noise matrix.

In the actual process of sound source identification, it is usually to inversely calculate matrix $\boldsymbol{S}(\omega)$ under the condition of knowing the microphone signal matrix $\boldsymbol{P}(\omega)$ [19]. In CBF, the frequency domain form of the microphone signal is used as the input, and the beamforming output of the sound source plane is calculated by using the steering vector pointing to the position $\boldsymbol{r}_n$. This method can be expressed as

$$y(\boldsymbol{r}_n, \omega) = \boldsymbol{w}^{\mathrm{H}}(\boldsymbol{r}_n, \omega)\boldsymbol{P}(\omega), \tag{5}$$

where $y(\boldsymbol{r}_n, \omega)$ represents the beamforming output; $\boldsymbol{w}^{\mathrm{H}}(\boldsymbol{r}_n, \omega)$ is the steering vector; and the superscript H indicates the conjugate transpose of a matrix,

$$\boldsymbol{w}(\boldsymbol{r}_n, \omega) = \frac{1}{M}\left[\frac{r_{1,n}}{4\pi}\mathrm{e}^{-\mathrm{j}\omega r_{1,n}/c} \quad \cdots \frac{r_{M,n}}{4\pi}\mathrm{e}^{-\mathrm{j}\omega r_{M,n}/c}\right]^{\mathrm{T}}. \tag{6}$$

Finally, the source strength information at any position on the sound source surface can be extracted from the sound pressure data received by the microphone through Eq. (5). However, the acoustic image of the sound source plane obtained at this time is still rather blurry. This is mainly attributed to the low spatial resolution of the reconstructed sound source distribution image and the false source phenomenon caused by the side lobe effect [20]. Therefore, it is necessary to further process the blurred image to improve the accuracy of sound source localization.

2.2 DAMAS

To further improve the spatial resolution of sound source identification, the DAMAS method decouples the aliased energy information between different spatial positions in the observation map. By adopting a deconvolution strategy, it restores a sound source image that is closer to the true distribution from the low—resolution observation results [21]. The correlation of sound sources between different spatial positions can be obtained by calculating the cross-correlation power of the beamforming results at the corresponding positions.

$$Y_{n,n'}(\omega) = E\{y(r_n, \omega)\, y(r_{n'}, \omega)\} = \boldsymbol{w}_n^{\mathrm{H}} E\left\{\boldsymbol{X}\boldsymbol{X}^{\mathrm{H}}\right\} \boldsymbol{w}_{n'} = \boldsymbol{w}_n^{\mathrm{H}} \boldsymbol{R} \boldsymbol{w}_{n'}, \tag{7}$$

where $Y_{n,n'}(\omega)$ represents the cross-correlation power of the beamforming outputs of r_n and $r_{n'}$, indicating the correlation between sound sources at different spatial positions; $\boldsymbol{R} = \mathrm{E}\left\{\boldsymbol{X}\boldsymbol{X}^{\mathrm{H}}\right\}$ represents the cross-spectral matrix (CSM) between different microphone channels at frequency ω; $\boldsymbol{w}_{n'}$ and $\boldsymbol{w}_n^{\mathrm{H}}$ depend on the relative positions between the microphone channels and the sound source points and are independent of random variables, which can be factored out; $E\{\cdot\}$ represents the mathematical expectation.

Expansion of Eq. (7) gives

$$Y_{n,n} = E\left\{\boldsymbol{w}_n^{\mathrm{H}} \boldsymbol{G}\boldsymbol{S}\boldsymbol{S}^{\mathrm{H}}\boldsymbol{G}^{\mathrm{H}}\boldsymbol{w}_n + \boldsymbol{w}_n^{\mathrm{H}}\boldsymbol{\eta}\boldsymbol{\eta}^{\mathrm{H}}\boldsymbol{w}_n\right\} \tag{8}$$

Then the formation of the output for the wave numbers of N sound sources can be expressed as

$$Y_{n,n'} = \sum_{i=1}^{N}\sum_{j=1}^{N} A_{n,n',i,j} Q_{i,j} + \boldsymbol{w}_n^{H} \boldsymbol{R}_{\eta} \boldsymbol{w}_n^{'}, \tag{9}$$

$$A_{n,n',i,j} = \boldsymbol{w}_n^{\mathrm{H}} \boldsymbol{G}_i \boldsymbol{G}_j^{\mathrm{H}} \boldsymbol{w}_{n'}, \tag{10}$$

$$Q_{i,j} = \mathrm{E}\left\{\hat{s}_i \hat{s}_j\right\}, \tag{11}$$

$$\boldsymbol{R}_{\eta} = \mathrm{E}\left\{\boldsymbol{\eta}\boldsymbol{\eta}^{\mathrm{H}}\right\}, \tag{12}$$

where $A_{n,n',i,j}$ is the superimposed power distribution at positions n and n' caused by a unit point sound source placed at positions i and j; $Q_{i,j}$ represents the cross-correlation power between the i-th and j-th sound sources; $\boldsymbol{R}_{\eta}$ is the covariance matrix of the array noise. It is usually assumed that the self-noise of the microphone array is composed of M independent and identically distributed Gaussian processes with a common variance σ^2, and the term related to the microphone self-noise can be simplified to σ^2/M.

Moreover, the aerodynamic loads on the WTB that are related to the generation of sound sources have a relatively small correlation length [22], and the sound sources at different positions are uncorrelated, Eq. (9) can be further simplified as

$$Y_{n,n'} = \sum_{i=1}^{N} A_{n,n',i,i} Q_{i,i} + \frac{\sigma^2}{M}, \tag{13}$$

where N represents the number of effective sound sources. The variance of the actual microphone self-noise is relatively small and can be neglected. Based on the sparsity of the sound sources, only the diagonal elements of the point spread function are retained, thereby obtaining the standard DAMAS equation

$$\boldsymbol{Y} = \boldsymbol{A}\boldsymbol{Q}, \tag{14}$$

where $\boldsymbol{Y}$ represents the observation result of the sound source map, $\boldsymbol{A}$ represents the PSF (Point spread function) matrix, and $\boldsymbol{Q}$ represents the true sound source power distribution. Theoretically, the standard DAMAS equation can be obtained by solving the inverse of matrix $\boldsymbol{A}$ to get $\boldsymbol{Q}$. However, due to the limited number of channels in the microphone array, matrix $\boldsymbol{A}$ is severely rank-deficient, making this equation an underdetermined system of equations. Therefore, the Gauss-Seidel type iterative relaxation method described in reference [23] is usually adopted to solve Eq. (14) to estimate the sound source distribution.

Compared with the CBF method, the DAMAS method requires higher computational resources, including longer running time and greater memory usage. Reducing the computational time of the deconvolution process not only helps to reduce measurement costs but also enhances the system's capabilities in real-time display and online analysis. Therefore, how to reduce the computational load of deconvolution has become another key research issue besides improving the accuracy of sound source localization [24].

2.3 Signal Recovery Method Based on OMP

The OMP method is a technique that represents the original signal using a set of sparse source dictionary coefficients. As shown in Eq. (15), OMP approximates the original observation matrix $\boldsymbol{Y}$ with a limited number of sources to the greatest extent possible [25].

$$\boldsymbol{Y} = \sum_{\gamma \in \boldsymbol{\Gamma}} \boldsymbol{q}_\gamma \boldsymbol{A}_\gamma, \tag{15}$$

where $\boldsymbol{\Gamma}$ represents the index set of sparse sound source locations; γ represents the index of a certain sound source location; $\boldsymbol{q}_\gamma$ corresponds to the sound source contribution weight at the index position; $\boldsymbol{A}_\gamma$ represents the point spread function at the corresponding position.

Unlike the Matching Pursuit (MP) method [26], OMP projects the signal onto the subspace spanned by the current dictionary subset in each iteration, thereby jointly updating all the selected coefficients. Compared with the deconvolution method based on the Gauss-Seidel type relaxation, the signal recovery strategy adopted by OMP directly seeks a sparse solution with a few non-zero source points, which is more in line with the physical characteristic that the aerodynamic noise of wind turbines is sparsely distributed in space. This method can not only effectively suppress noise interference and reduce the occurrence of false sources, but also significantly reduce the overall computational complexity. The specific calculation process is as follows.

Step 1: Set the initial residual to the original fuzzy observation map $\rho^{(i-1)} = \boldsymbol{Y}$, the index set of the initial candidate sound source positions to $\boldsymbol{\Gamma} = \varnothing$, and $\boldsymbol{Q} = \boldsymbol{0}$ initialize the sound source contribution weight matrix.

Step 2: During the i-th iteration, calculate the index of the position that maximizes the contribution of the current point spread function in explaining the residuals

$$\gamma^{(i)} = \max_{\gamma \in \mathbf{\Gamma}} \left| A_{\gamma}^{H} \rho^{(i-1)} \right|, \tag{16}$$

where $\gamma^{(i)}$ is the grid point position most likely to contain the sound source in the i-th iteration; A_{γ}^{H} represents the conjugate transpose of the point spread function corresponding to the source location.

Step 3: Calculate the temporary contribution weight of the sound source $q_{\gamma^{(i)}}$ corresponding to this position

$$q_{\gamma^{(i)}} = \frac{A_{\gamma^{(i)}}^{H} \rho^{(i-1)}}{\left\| A_{\gamma^{(i)}} \right\|^{2}}. \tag{17}$$

Step 4: Re-fit the temporary contribution weights of the identified sound sources using the least—squares method. This is to ensure that the projection of the residual onto the subspace spanned by the selected contribution weights is zero. The orthogonalization process represented by Eq. (18)

$$\boldsymbol{q}^{(i)} = \underset{q}{argmin} \| \boldsymbol{Y} - \sum_{n=1}^{i} \boldsymbol{A}_{\gamma^{(n)}} q_{\gamma^{(n)}} \|^{2}. \tag{18}$$

The essence of Eq. (18) is to orthogonally project the signal onto the subspace spanned by the selected PSF, correct the weights at the determined source locations, and incorporate the corrected source weights into the source contribution weight matrix.

Step 5: Update the residuals by removing the explained Y from the original residuals

$$\rho^{(i)} = \boldsymbol{Y} - \sum_{n=1}^{i} \boldsymbol{A}_{\gamma^{(n)}} q_{\gamma^{(n)}}. \tag{19}$$

Step 6: Continue to execute the process from steps 2 to 5 until the residual reaches the set level or the number of iterations reaches the set value. The final source weight matrix can be expressed as

$$\boldsymbol{Q}_{\Gamma} = \boldsymbol{A}_{\Gamma}^{\dagger} \boldsymbol{Y}, \tag{20}$$

where $\boldsymbol{Q}_{\Gamma}$ represents the source contribution weight matrix sparsely expressed by the elements in set $\mathbf{\Gamma}$ and $(\cdot)^{\dagger}$ represents the Moore-Penrose pseudo-inverse.

2.4 TD Method for Rotating Sound Sources

Compared with a stationary sound source, the position and velocity of a rotating sound source change over time, and the relative position between the sound source and the microphone also varies with time. This dynamic change leads to the Doppler effect of the moving sound source, causing the frequency and amplitude of the sound field signal received by the microphone to deviate from the original sound source information [27]. Therefore, this paper introduces the TD method [28] to compensate for the Doppler effect caused by the rotating sound source. When the sound source changes from a stationary state to a rotating motion state, Eq. (1) is adjusted accordingly as

$$p\left(\boldsymbol{r}_m, t\right) = \sum_{n=1}^{N} \frac{r_0}{\left\| \boldsymbol{r}_m - \boldsymbol{r}_n\left(\tau\right) \right\| \left| 1 - \mathcal{M}_{mn}\left(\tau\right) \right|} s_n \left(t - \frac{\left\| \boldsymbol{r}_m - \boldsymbol{r}_n\left(\tau\right) \right\|}{c} \right), \tag{21}$$

where $\boldsymbol{r}_n(\tau)$ represents the position vector of sound source n at time τ; τ indicates the emission time of the sound source; t represents the reception time of the microphone; and $\mathcal{M}_{mn}(\tau)$ denotes the projection of the Mach number of the tangential velocity vector $\boldsymbol{v}(\tau)$ onto the radiation vector at the emission time of the sound source,

$$\mathcal{M}_{mn}(\tau) = \frac{(\boldsymbol{r}_m - \boldsymbol{r}_n(\tau))}{\|\boldsymbol{r}_m - \boldsymbol{r}_n(\tau)\|} \cdot \frac{\boldsymbol{v}(\tau)}{c}. \tag{22}$$

The relationship between the emission frequency of the moving sound source and the receiving frequency of the microphone is

$$\omega_m = \frac{\omega_n}{1 - \mathcal{M}_{mn}(\tau)}, \tag{23}$$

where ω_{n} represents the emission frequency of the sound source and ω_{m} represents the receiving frequency of the microphone m.

As the scanning plane needs to rotate synchronously with the sound source, the position of grid point n varies with time. At time τ, this position is determined by the rotational speed Ω of the sound source

$$\boldsymbol{r}_n(\tau) = \begin{bmatrix} x_n \cos\theta(\tau) - y_n \sin\theta(\tau) \\ x_n \cos\theta(\tau) + y_n \sin\theta(\tau) \\ z_n \end{bmatrix}, \tag{24}$$

where x_n, y_n, z_n is the coordinates of the sound source at the initial moment τ_0; $\theta(\tau) = \Omega(\tau - \tau_0)$ is the angle through which the sound source has turned.

The sound source signal at point $\boldsymbol{r}_n$ can be reconstructed in the time domain to remove Doppler effect based on the time-domain acoustic pressure signal of the microphone m as follows

$$s_{mn}(\tau) = \left[\frac{1}{4\pi\|\boldsymbol{r}_m - \boldsymbol{r}_n(\tau)\| \cdot |1 - \mathcal{M}_{mn}(\tau)|}\right]^{-1} \tilde{p}(\boldsymbol{r}_m, t). \tag{25}$$

In the context of calculation, the value of $\tilde{p}(\boldsymbol{r}_m, t)$ does not exactly coincide with the sampling instants. Suppose that t falls precisely between the sampling instants t_i and t_{i+1}. Then, the time-domain acoustic pressure signal of the microphone at time t can be obtained via linear interpolation as

$$\tilde{p}(r_m, t) = \begin{cases} \dfrac{t - t_i}{1/F_s} x(\boldsymbol{r}_m, t_i) + \dfrac{t_{i+1} - t}{1/F_s} p_m(\boldsymbol{r}_m, t_{i+1}), & t_i \le t \le t_{i+1} \\ 0 & \text{, otherwise} \end{cases} \tag{26}$$

where F_s denotes the sampling rate of the microphone. In the subsequent step, the reconstructed time-domain acoustic pressure signal can be partitioned into D segments. For the signal of each segment, FFT (Fast Fourier transform) is carried out.

Consequently, the spectrum of the acoustic pressure signal can be estimated as

$$y_{nm}^{(d)}(\omega) = F\left\{s_{nm}^{(d)}(\tau)\right\}, \tag{27}$$

where d represents any segment, $d = [1, 2, \cdots, D]$. The weighted sum of the spectral results of all M microphones is taken to obtain the beamforming output at a certain frequency ω as

$$\boldsymbol{y}_n^{(d)}(\omega) = \frac{1}{M}\sum_{m=1}^{M} y_{nm}^{(d)}(\omega). \tag{28}$$

According to Eq. (27), the cross-correlation power between any positions i and j of the d segment arbitrary sound source surface can be calculated

$$\boldsymbol{Y}^{(d)}{}_{ij}(\omega) = E\left[\boldsymbol{y}_i^{(d)}(\omega) \cdot \boldsymbol{y}_j^{(d)}(\omega)^H\right]. \tag{29}$$

Finally, the weighted average of section D yields the cross-correlation power between i and j as

$$\boldsymbol{Y} = \frac{1}{D}\sum_{d=1}^{D} \boldsymbol{Y}_{ij}^{(d)}(\omega). \tag{30}$$

By substituting the calculation results of Eq. (29) into Eq. (13), the standard input $\boldsymbol{Y}$ of the DAMAS method can be obtained. Even though the TD-BF can effectively rectify the amplitude and phase distortions of the microphone signals induced by the motion of the sound source, $\boldsymbol{Y}$ still manifests as a blurred sound source image. Consequently, it is necessary to further process it as the input of the OMP-DAMAS algorithm to acquire a clearer sound source imaging result. Algorithm 1 is as follows:

Algorithm 1: TD-OMP-DAMAS

1: **Input:** Microphone coordinates for all channels of the array $\boldsymbol{r}_m\ (m = 1, 2, \ldots, M)$, sample frequency F_s, Coordinates of all grid points on the scanning surface of the sound source $\boldsymbol{r}_n\ (n = 1, 2, \ldots, N)$, target frequency for imaging ω, time axes $\boldsymbol{t} = [0, 1, \ldots L-1]$, microphone signals $\boldsymbol{p}(\boldsymbol{r}_m, \boldsymbol{t}) \in \mathbb{R}^{L*M}$, angular speed Ω, reference time $\tau_0 = 0$. residual e, Number of iterations u.
2: Initialize the observation result of the sound source map matrix $\boldsymbol{Y} = \boldsymbol{0}$.
3: **For** $d =$ 1:C do
Calculate the turned angle $\theta(\tau)$;
For $n =$ 1: N do
obtain the position vector $\boldsymbol{r}_n(\tau)$ according to Eq. (24);
For $m =$ 1:M do
Calculate Pointing vector $\boldsymbol{r}_m - \boldsymbol{r}_n(\tau)$, Euclidean distance $\|\boldsymbol{r}_m - \boldsymbol{r}_n(\tau)\|$, the tangential velocity vector $\boldsymbol{v}(\tau)$ and the Mach number $\mathcal{M}_{mn}(\tau)$;
Construct receiving sound pressure$\tilde{p}(\boldsymbol{r}_m, t)$ according to Eq. (26);
Obtain sound source signal $s_{mn}(\tau)$ by the Eq. (25);
End for m
Calculating amplitude $\boldsymbol{y}_n^{(d)}(\omega)$ according to Eq. (28);
End for n
Obtain average power $\boldsymbol{Y}^{(d)}{}_{ij}(\omega)$ by the Eq. (29);
End for d.
4: Update $\boldsymbol{Y}$ according to Eq. (30).
5: Calculate the point spread function matrix $\boldsymbol{A}$.
6: Initialize $\rho^{(i-1)} = \boldsymbol{Y}$, $\boldsymbol{\Gamma} = \varnothing$, $\boldsymbol{Q} = \boldsymbol{0}$.

(Continued)

Algorithm 1 (continued)

7: **For** $i = 1: u$ do
Compute the grid point position most likely to contain the sound source in the current iteration $\gamma^{(i)}$ by the Eq. (16);
Calculate $q_{\gamma^{(i)}}$ according to Eq. (17);
Update $q_{\gamma^{(i)}}$ by the Eq. (18);
Update the remaining residuals $\rho^{(i)} = \boldsymbol{Y} - A_{\gamma^{(i)}} q_{\gamma^{(i)}}$;
Update $i = i + 1$
Construct $\boldsymbol{Q} = \boldsymbol{Q} + q_{\gamma^{(i)}}$
Calculate $\boldsymbol{\Gamma} = \gamma^{(i)} \cup \boldsymbol{\Gamma}$
If $\rho^{(i)} \leq e$ then
Break
End if
End for i.
8: **Output:** $\boldsymbol{Q}$ and $\boldsymbol{\Gamma}$.

3 Numerical Simulations

3.1 Simulation Parameters

To evaluate the performance of the proposed algorithm, three monopole sound sources arranged with a 120° phase separation were simulated, as illustrated in Fig. 2. The sources rotated counterclockwise around the y-axis in the XOZ plane with a radius of 0.4 m and an equivalent amplitude of 1 Pa. Their frequencies were set to 500, 1500, and 2500, respectively, and the rotational speed Ω was 750 r/min. The sound-source region was defined as a 0.6 × 0.6 m rectangular plane. Considering the array aperture of 1.7 m, the test distance of 2 m, and the target frequency range of 1000–2500 Hz, the Rayleigh criterion yields a theoretical spatial resolution of approximately 0.25–0.5 m. To avoid spatial aliasing while maintaining computational efficiency, reference [29] recommends that the ratio between grid spacing and spatial resolution remain within the interval [0.05,0.2]. Following this guideline, a grid spacing of 0.05 m was selected for the simulation.

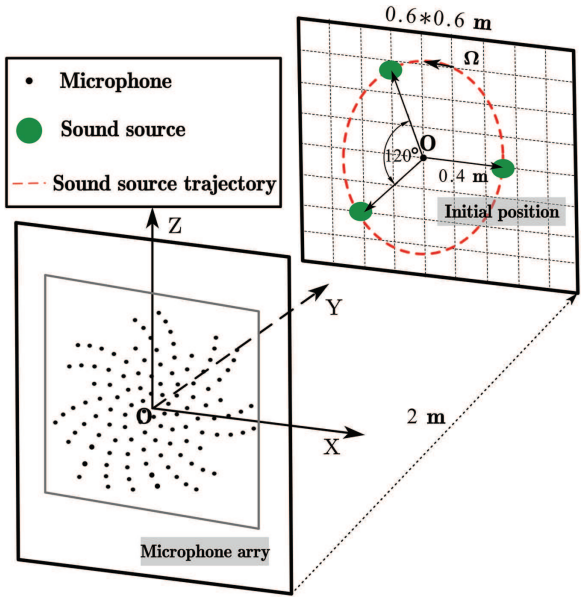

Figure 2: Simulation experiment of rotating point sound source

Under comparable array apertures and grid densities, traditional deconvolution algorithms typically require approximately 1000 iterations to reach convergence for complex source distributions [30]. However, to balance convergence performance with computational efficiency, the initial maximum iteration count in this study was set to 200. Because OMP assumes sparsity in the underlying sound sources, its stopping criterion is primarily governed by a predefined residual threshold, and the maximum number of iterations should generally exceed the expected number of sources to ensure that all active components are detected. Therefore, increasing the allowable maximum iteration count does not substantially raise computational costs while helping avoid premature termination. In this work, the algorithm is considered converged when the residual norm decreases below 1×10^{-3}.

Regarding the analysis duration, the algorithm requires the data segment to contain at least one full rotation period to ensure accurate time-domain Doppler compensation. Although extending the time window can improve the signal-to-noise ratio and enhance statistical stability, an excessively long duration may obscure the non-stationary characteristics of the rotating sound sources. To balance the suppression of measurement noise with the preservation of dynamic source features, a data segment spanning ten rotation periods (10T) was selected for processing and analysis.

The simulation array was positioned on the plane $y = 2$ m and configured with 112 microphone channels operating at a sampling rate of 48 kHz. The array center was aligned with the rotation center of the monopole sources. To evaluate robustness under different noise conditions, uncorrelated Gaussian white noise was added independently to each channel, yielding signal-to-noise ratios (SNRs) ranging from –10 to 20 dB in 3 dB increments. All computations were performed under identical hardware conditions (CPU: Intel i7-8850H; memory: 16 GB). For consistent comparison across methods, the reconstructed acoustic maps were normalized to 0 dB with a dynamic range of 10 dB.

3.2 Simulation Result

The localization results at an SNR of 11 dB are summarized in Table 1. Each row reports the performance at 1000, 1500, and 2500 Hz, while each column corresponds to one of the four methods along with the reconstructed source maps. In the figures, the true source positions are marked by black "×" symbols, and the estimated positions are indicated by red "o" markers. At 1000 Hz, the conventional CBF method exhibits an extremely broad mainlobe accompanied by strong sidelobe contamination, making it difficult to distinguish the three closely spaced rotating monopoles. Although TD-BF alleviates Doppler-induced distortions through time-domain resampling, its spatial resolution remains limited at low frequencies due to the relatively small effective array aperture. In contrast, both TD-DAMAS and TD-OMP-DAMAS effectively suppress spatial energy leakage and produce markedly sharper mainlobe peaks. At higher frequencies (1500 and 2500 Hz), this advantage becomes increasingly evident: TD-DAMAS achieves clear separation of the three sources, while TD-OMP-DAMAS delivers the most compact, accurately localized, and interference-free source distributions among all tested methods.

Table 1: The results of sound source localization for three rotating sound sources

Methods	Frequencies		
	1000 Hz	1500 Hz	2500 Hz
CBF	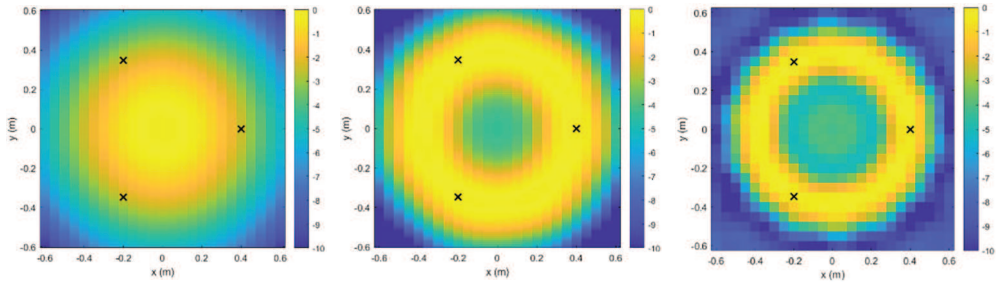		
TD-BF	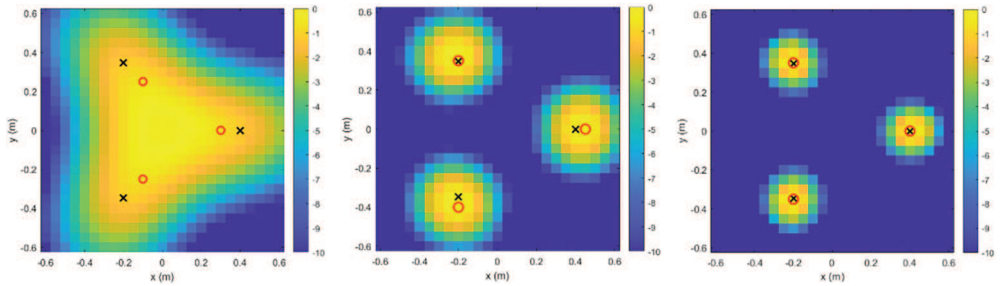		
TD-DAMAS	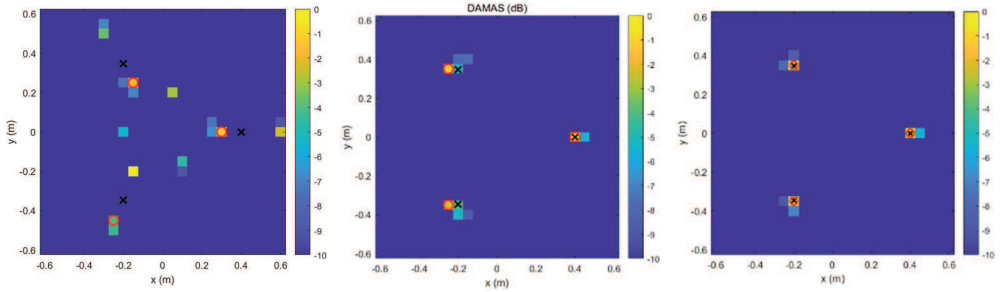		
TD-OMP-DAMAS	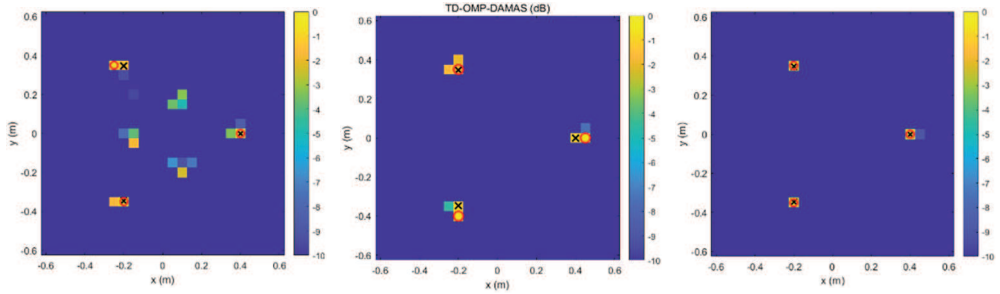		

Fig. 3a shows the 3 dB horizontal beamwidths at 1000 Hz under an SNR of −10 dB [31]. In the presence of strong noise contamination, the CBF beamwidth expands far beyond the true source region, making it impossible to distinguish multiple sources from the reconstructed maps. Although TD-BF compensates for Doppler-induced spectral distortion, its beamwidth remains excessively wide due to limited array resolution at low frequencies. In contrast, the sparsity-constrained framework of TD-OMP-DAMAS yields the narrowest beamwidth among all methods, demonstrating that deconvolution-based approaches substantially enhance spatial resolution and provide superior robustness under low-SNR conditions. Fig. 3b compares the convergence characteristics of TD-DAMAS and TD-OMP-DAMAS. The TD-DAMAS residual

decreases steadily but slowly, requiring more than 150 iterations to reach a quasi-steady level. For the present simulation configuration, the computational complexity of TD-OMP-DAMAS is of the same order of magnitude as TD-DAMAS (FLOPs: 1.03×10^8 vs. 7.81×10^7). Although each iteration of TD-OMP-DAMAS incurs slightly higher computational cost, it converges to a substantially lower residual within approximately 65 iterations, whereas TD-DAMAS still requires more than 150 iterations to stabilize. Thus, for a given reconstruction accuracy, TD-OMP-DAMAS demonstrates markedly faster convergence and produces higher-quality source maps without increasing the overall computational burden. Fig. 3c presents the localization errors—computed using Eq. (31)—for the four methods across different SNR levels. As the SNR increases, all methods exhibit decreasing localization error. TD-OMP-DAMAS consistently achieves the lowest error across the entire SNR range. Notably, TD-DAMAS also exhibits significantly higher robustness than CBF and TD-BF under low-SNR conditions.

$$Error = \frac{1}{N}\sum_{n=1}^{N}\frac{\left|\sqrt{\tilde{x}_n^2+\tilde{z}_n^2}-\sqrt{x_n^2+z_n^2}\right|}{\sqrt{x_n^2+z_n^2}} \times 100\% \tag{31}$$

where x_n, z_n is the true position of the sound source; $\tilde{x}_n$, $\tilde{z}_n$ is the position identified by the algorithm.

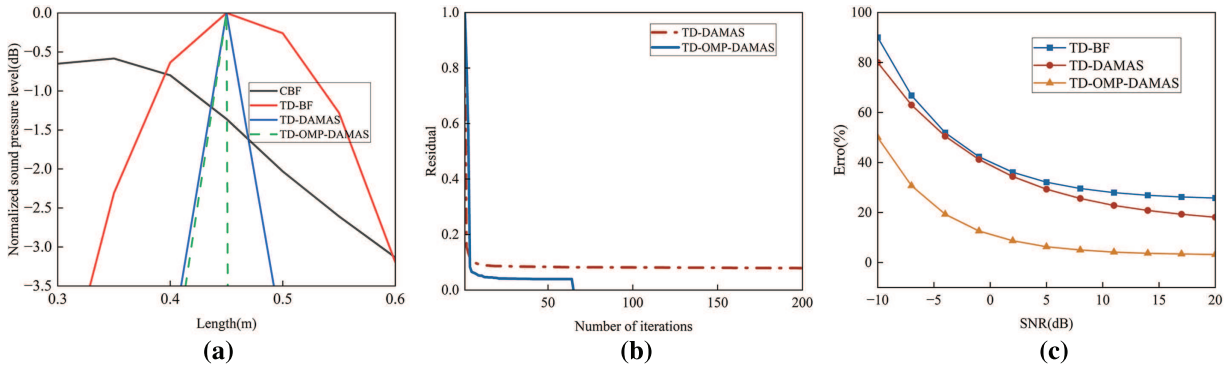

Figure 3: Algorithm performance evaluation: (**a**) 3 dB horizontal beamwidths of different algorithms at SNR = −10 dB, frequency is 1000 Hz; (**b**) Convergence of different algorithms at SNR = −10 dB; (**c**) Localization error of the algorithm at different SNRs when the source frequency is 1000 Hz

4 Experimental Evaluation

We evaluated the proposed methods using two experiments. One was a location identification experiment of three rotating sound sources with the same frequency, which aimed to evaluate the resolution and performance of the TD-OMP-DAMAS algorithm. The other experiment involved the application of the algorithm in the field of wind turbine aerodynamic noise location identification. The purpose of this experiment was to assess the application potential of the algorithm in the field of wind turbine aerodynamic acoustic identification, study the evolution law of wind turbine aerodynamic noise under different working conditions, and provide high-resolution sound source images for wind turbine noise reduction design.

4.1 Experimental Equipment

The rotating simulation platform employed in the experiments consisted of a Y90S-4 three-phase asynchronous motor, a rotating shaft, a frequency converter, and fixing devices. The rotating disk had a diameter of 1.2 m and a thickness of 0.05 m for the rotating surface. On its front side, circumferential radius scales in millimeters were marked, and the disk was partitioned into a circular calculation field point model with 360 × 6 points. During the experiments, a piezoelectric crystal buzzer with a frequency of 2543 Hz was

utilized as a sound source device. The acoustic signals were acquired using an 112-channel microphone array. The array had a diameter of 1.7 m, with a frequency acquisition range spanning from 0.01 to 24 kHz and a sampling frequency of 48 kHz, thus satisfying the experimental requirements of this research. As depicted in Fig. 4a, the experimental setup is illustrated. Fig. 4c shows the frequency spectrum comparison between a stationary point sound source and a rotating point sound source. For each experiment, the data recording duration was set to 10 s, and three sets of data were collected under each working condition to enhance the reliability of the experimental outcomes.

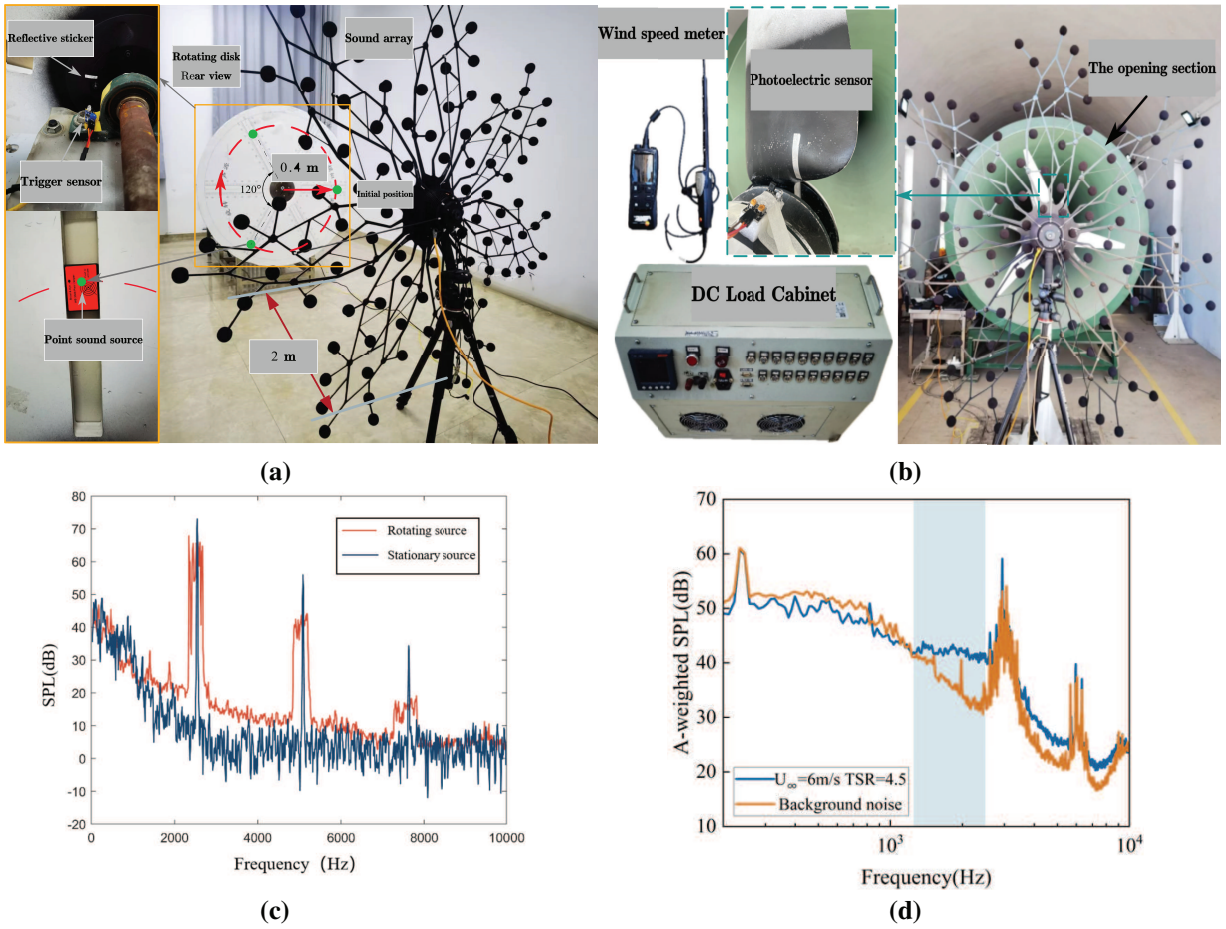

Figure 4: Experimental setup and signal spectrum diagrams: (**a**) Schematic diagram of the rotating stand experiment setup; (**b**) Schematic diagram of the wind tunnel experiment setup; (**c**) Frequency spectrum comparison between a stationary point sound source and a rotating point sound source; (**d**) The background noise of wind tunnels and the frequency spectrum of wind turbine noise

The experiments were conducted in a B1/K2 wind tunnel with an overall length of 24.59 m. The facility consists of a drive section, a flow-conditioning section, a contraction section, a closed test section, a diffuser, and an open-jet test section. The diameter of the open-jet test section is 2.04 m, and the incoming flow turbulence intensity is below 4%. The tunnel can provide a steady freestream velocity of up to 20 m/s. Detailed specifications of the model wind turbine are listed in Table 2. Prior to the experiments, the freestream velocity in the open-jet test section was calibrated using a hot-wire anemometer with a measurement range of 0–20 m/s and a resolution of 0.01 m/s. The calibration conditions are summarized in Table 3. The electrical

load of the turbine motor was adjusted using a DC electronic load unit to achieve different tip-speed ratios under the same inflow velocity.

Table 2: Wind turbine parameters

Parameters	Value
Number of blades	3
Blade length	0.70 m
Chord length at the blade tip	0.04 m
Airfoil section	SD2030
Rated power	400 W
Rated wind speed	10 m/s
Rated speed	750 r/min
Starting wind speed	3 m/s
Blade material	Wooden + glass fiber

Table 3: Wind tunnel experiment conditions

Wind speed (m/s)	Tip speed ratio	The linear velocity at the blade tip (m/s)	The rotational speed of the wind turbine (r/min)
6	4.5	17	368.3
6	5	30	409.3
6	5.5	33	450.2
6	6	36	491.1
7	4.5	31.5	429.7
7	5	35	477.5
7	5.5	38.5	525.2
7	6	42	573.0
8	4.5	36	491.1
8	5	40	545.7
8	5.5	44	600.2
8	6	48	654.8
9	4.5	40.5	552.5
9	5	45	613.9
9	5.5	49.5	675.3
9	6	54	736.7
10	4.5	45	613.9
10	5	50	682.1
10	5.5	55	750.3
10	6	60	818.5

The rotor speed and blade phase angle were measured using a photoelectric sensor in combination with a reflective marker. As illustrated in Fig. 4b, the photoelectric sensor was mounted behind the rotor on the top of the nacelle to minimize the influence of the incoming flow on measurement accuracy. A reflective

marker was attached to one blade—designated as Blade 1—and the sensor trigger position was defined as a phase angle of 0°. For each operating condition, three measurement runs were performed, with each run lasting 10 s. Fig. 4d shows the background noise measured in the wind tunnel and the frequency spectrum of the wind turbine noise.

4.2 Multi-Rotation Sound Source Verification of Algorithms

Fig. 5a–d presents the source imaging results of the four methods applied to the measured three-rotating-source data. The CBF map exhibits a pronounced ring-shaped pattern accompanied by strong sidelobe artifacts. As shown in Fig. 4c, rotating sources undergo Doppler frequency shifts, spectral broadening, and amplitude/phase modulation. These effects introduce phase inconsistencies across array channels, which intensify energy aliasing among multiple sources and significantly degrade the spatial resolution of CBF, making it unable to correctly distinguish the three source positions. TD-DAMAS can separate the three sources to some extent; however, substantial spatial energy diffusion remains visible in the reconstructed map. In contrast, TD-OMP-DAMAS first restores instantaneous phase coherence among array elements via time-domain Doppler correction, thereby mitigating the spatial defocusing caused by Doppler-induced spectral broadening. It then applies OMP-based sparse reconstruction, which imposes strong sparsity constraints so that only atoms most correlated with the true sources are retained. This fundamentally suppresses sidelobe formation and spreading energy. Through the combination of accurate time-domain Doppler compensation and sparsity-constrained deconvolution, TD-OMP-DAMAS achieves markedly improved spatial resolution, producing sharper and more concentrated source peaks. These results clearly demonstrate the superior localization capability of the proposed method in complex multi-rotating-source scenarios.

Fig. 6a illustrates the evolution of the residuals for TD-OMP-DAMAS and TD-DAMAS during the iterative process. TD-DAMAS exhibits the fastest initial decrease, with its rapidly dropping and stabilizing within only a few iterations. In contrast, TD-OMP-DAMAS undergoes more substantial adaptive refinement of its sparse structure in the early stage, resulting in a slower initial decrease. However, after approximately 50 iterations, it converges rapidly to a much lower steady-state residual, indicating superior sparse-reconstruction capability and improved source-focusing accuracy. Fig. 6b compares the average localization errors of the three methods. TD-BF shows the poorest performance, with an average error of approximately 15.6% and the largest standard deviation. This indicates that TD-BF is highly sensitive to noise and variations in experimental conditions, leading to large fluctuations across repeated measurements and poor repeatability. In contrast, TD-DAMAS effectively suppresses sidelobe interference through deconvolution, reducing the average error to about 5.9% and substantially decreasing the standard deviation. This demonstrates that deconvolution not only mitigates sidelobes and noise sensitivity but also enhances consistency and repeatability across experimental conditions. TD-OMP-DAMAS further improves localization performance through the combined benefits of time-domain Doppler correction and OMP-based sparse reconstruction. It achieves the highest accuracy among the three methods, with the average error reduced to 4.2%, and simultaneously yields the smallest variance, confirming its robustness and excellent repeatability in complex measurement environments. Fig. 6c compares the horizontal beamwidths of the three methods. TD-BF exhibits the widest beamwidth with shallow edge transitions, corresponding to the lowest spatial resolution. TD-DAMAS significantly narrows the beamwidth and improves source discrimination. TD-OMP-DAMAS, however, achieves the sharpest and most concentrated beamwidth with the strongest sidelobe suppression, providing superior spatial resolution compared with both TD-BF and TD-DAMAS.

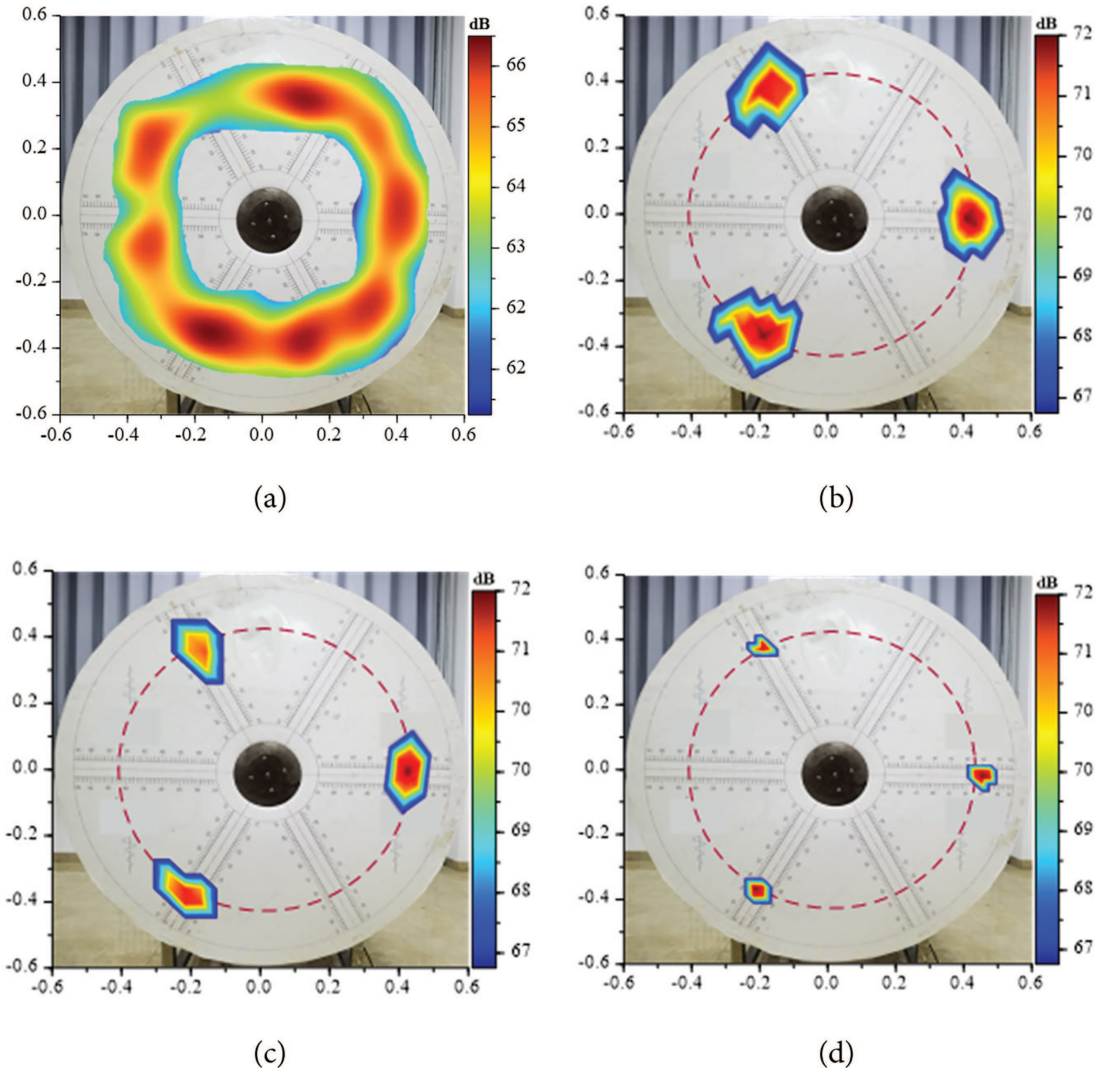

Figure 5: The source identification results of different algorithms under the working conditions of a sound source frequency of 2534 Hz, a rotational speed of 270 r/min, and a rotational radius of 0.4 m: (**a**) CBF; (**b**) TD-BF; (**c**) DAMAS; (**d**) TD-OMP-DAMAS

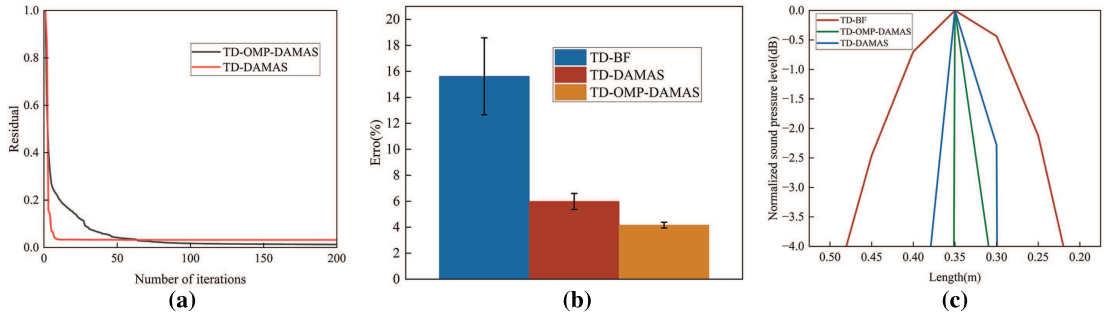

Figure 6: Comparison of recognition performance of different algorithms at a rotational speed of 270 r/min and a sound source frequency of 2543 Hz: (**a**) Convergence rate comparison between TD-DAMAS and TD-OMP-DAMAS; (**b**) Comparison of positioning errors of different algorithms; (**c**) 3 dB horizontal beamwidths

4.3 Identification and Analysis of Aerodynamic Noise from Wind Turbine

As shown in Fig. 4d, when the incoming wind speed is 6 m/s and the tip speed ratio is 4.5, the A-weighted sound pressure level of the wind turbine is mainly affected by the background noise, among which the broadband noise at 3 kHz and its harmonics caused by the wind tunnel strainer are the main components. After eliminating the interference of the wind tunnel background noise, it can be found that the frequency band with higher aerodynamic noise energy of the wind turbine mainly concentrates in the range of 1.2–2.5 kHz. The background noise in the wind tunnel is mainly removed by a band-pass filter with a cut-off frequency of 1.2–2.5 kHz. Subsequently, any section of the filtered signal is selected for FFT analysis, and the frequency corresponding to the maximum sound pressure level is extracted as the target frequency. The sound source surface is set to 1 m × 1 m, the spatial grid spacing is set to 0.02 m, the convergence residual threshold is set to 1×10^{-3}, and the maximum number of iterations is set to 1000. Fig. 7a–d shows the average values of the aerodynamic sound source identification results of the three algorithms in this frequency band when the WTB rotates 10T. Table 4 compares the required calculation time and main lobe width of different algorithms. The results show that the calculation times of the TD-BF algorithm, TD-DAMAS algorithm and the improved TD-OMP-DAMAS algorithm are 10.10, 10,055.35 and 3117.26 s, respectively. Taking the 3 dB horizontal beamwidth of TD-OMP-DAMAS as the reference, the relative 3 dB horizontal beamwidths of other methods were calculated. The results show that the relative main lobe areas of the CBF algorithm and the TD-DAMAS algorithm are 9.75 and 2.25, respectively. Compared with CBF, the improved TD-OMP-DAMAS algorithm has an 89% improvement in spatial resolution; compared with TD-DAMAS, the calculation time is reduced by 69%. Therefore, TD-OMP-DAMAS demonstrates superior identification performance in the identification of wind turbine aerodynamic noise sources.

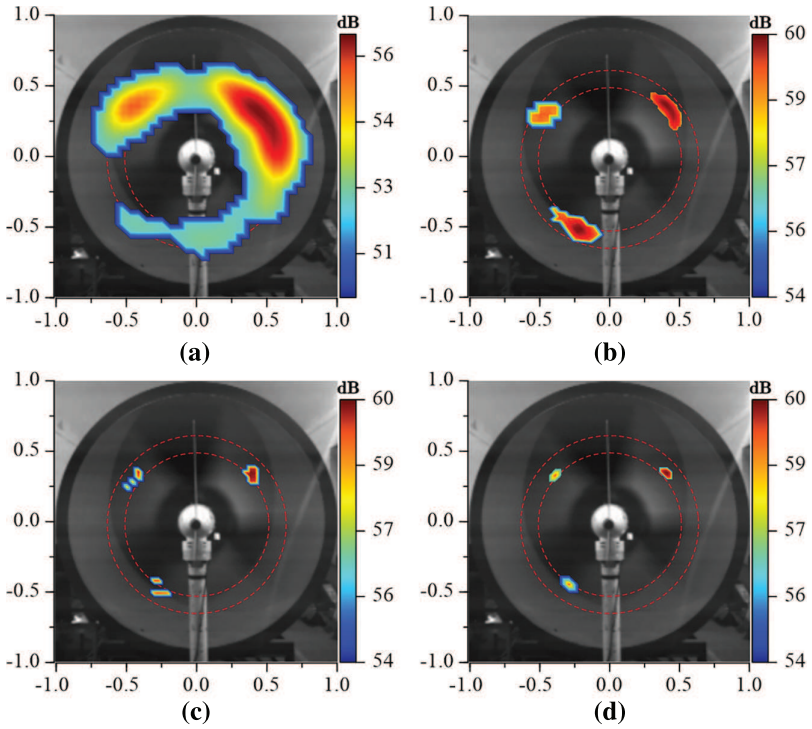

Figure 7: The identification results of aerodynamic noise of wind turbines under different algorithms when the wind speed is 6 m/s, the tip speed ratio is 4.5, and the rotational speed is 368.3 r/min: (**a**) CBF; (**b**) TD-BF; (**c**) DAMAS; (**d**) TD-OMP-DAMAS

Table 4: Computational performance of different methods

Methods	CBF	TD-DAMAS	TD-OMP-DAMAS
Times (s)	10.10	10,055.35	3117.22
Relative 3 dB horizontal beamwidths	9.75	2.25	1

It can be discerned from Fig. 8a that under diverse incoming wind speed conditions, the aerodynamic noise of WTB is predominantly concentrated within the radial interval of 0.50 to 0.56 m, corresponding to the spanwise range of 0.71–0.78 R. Moreover, as the wind speed escalates, the radial position associated with the maximum acoustic energy gradually shifts towards the blade tip. The emergence of this phenomenon can be primarily ascribed to the centrifugal force experienced by the fluid, along with the presence of streamwise vortices and hairpin vortex structures identified in the investigation of flow characteristics in similar wind turbines as reported in Reference [32]. On one hand, the streamwise vortices and hairpin vortex structures lead to a notable augmentation of the pressure difference within this region, thereby triggering substantial fluctuations in the pressure coefficient. In accordance with the generation mechanism of aerodynamic noise in WTB [33], a positive correlation exists between the magnitude of the pressure difference and the intensity of the sound source. Consequently, this region becomes the principal locus of acoustic energy concentration. On the other hand, during the evolutionary process of hairpin vortices, a fluid ejection phenomenon transpires [34]. This ejection instigates intense momentum exchange among the surrounding fluid, subsequently facilitating the fragmentation of hairpin vortices. This, in turn, gives rise to random pressure pulsations in the local fluid, ultimately culminating in the formation of broadband noise. Furthermore, observations have also revealed that the distribution of aerodynamic noise energy across the WTB is non-uniform. The relatively maximum acoustic energy is observed at the upward—moving position of the blade, a finding that aligns precisely with the research conclusions presented in Reference [35]. It is hypothesized that the underlying reason for this lies in the fact that during the upward motion of the blade, the direction of motion runs counter to the direction of gravitational acceleration. This results in a diminution of the tensile effect of the gravitational load along the spanwise direction and an enhancement of the intensity of flapwise vibration [36]. Therefore, the intensity of the sound source of this blade surpasses that of the other two blades in the downward-moving state.

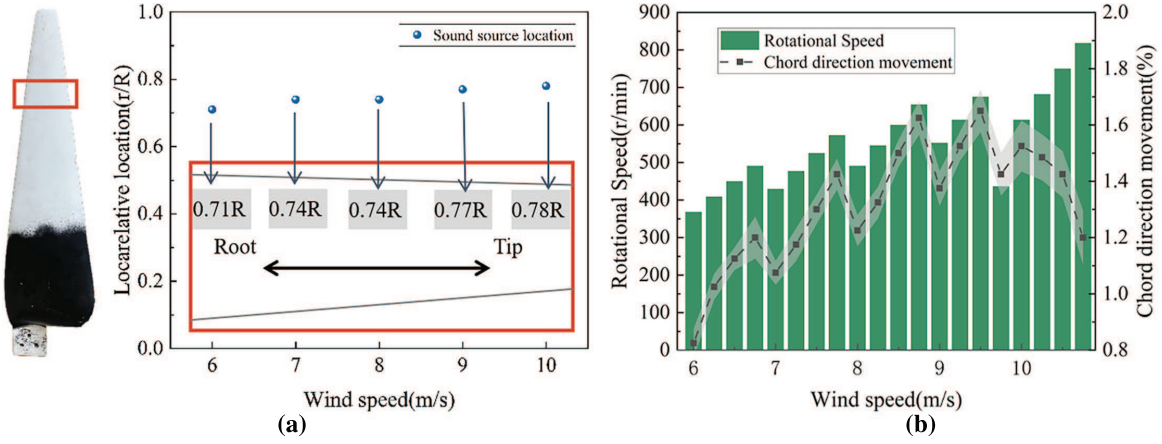

Figure 8: Wind tunnel test results: (**a**) Radial position variation of the aerodynamic sound source of the WTB under different operating conditions; (**b**) The directional position variation of the WTB sound source

With the distance between the noise source identified at a wind turbine rotational speed of 368.3 rpm and the trailing edge of the blade designated as the reference value, Fig. 8b depicts the chord-wise displacement ratio of this distance to the reference value under various rotational speeds. It can be observed that when the incoming wind speed is no greater than 10 m/s, the tendency of the maximum sound-energy position to shift along the chord from the leading edge to the trailing edge is strongly correlated with the rotational speed. Specifically, as the rotational speed increases, the maximum sound-energy position moves towards the leading edge; conversely, it migrates towards the trailing edge. However, when the incoming wind speed attains 10 m/s, with the increase in rotational speed, the position of the sound source starts to move in the direction of the trailing edge. Overall, the position of the sound source along the chord-wise direction exhibits a trend of first moving towards the leading edge and then towards the trailing edge as the rotational speed rises. It reaches the maximum displacement at a rotational speed of 675 rpm, with the maximum chord-wise displacement ratio being 2.35%. This phenomenon is primarily attributable to the alteration in the ejection position of the hairpin vortex at the trailing edge of the WTB. The rotational movement of the WTB subjects the air flow on the blade surface to the combined influence of the Coriolis force and the centrifugal force [37]. At relatively low rotational speeds, the chord-wise component of the centrifugal force (directed towards the leading edge) assumes a dominant role. When the rotational speed increases to a certain level, the Coriolis force gradually governs the fluid motion. As a result, under the action of the Coriolis force, the hairpin vortex moves along the chord towards the trailing edge.

5 Conclusions

This paper proposes a rotation sound-source identification method, TD-OMP-DAMAS, which achieves both high spatial resolution and high computational efficiency, enabling effective separation of aerodynamic noise generated by different wind turbine blades. The method operates by first applying time-domain resampling to compensate for Doppler effects induced by rotating sources. Then, leveraging the inherent sparsity of aerodynamic noise distributions, the spatial resolution is substantially enhanced through sparse modeling, iterative correlation-based atom selection, and non-negative back-substitution.

The performance of the proposed method was validated through comprehensive simulations and compared against CBF, TD-BF, and TD-DAMAS. Quantitative evaluations in terms of localization error and mainlobe width demonstrate that TD-OMP-DAMAS provides superior accuracy, robustness, and convergence speed. Under multi-rotating-source conditions, it delivers the best identification capability among all methods examined. Overall, this study addresses the existing gap in the applicability of sparse-reconstruction techniques to rotating sound-source scenarios. The proposed method accurately separates the noise contributions of individual blades even under challenging conditions, including strong Doppler effects, multi-source coupling, and complex acoustic environments, demonstrating excellent resolution and robustness. It is expected to offer a novel and practical technical route for single-blade-level fault diagnosis of wind turbines based on acoustic measurements.

In addition, TD-OMP-DAMAS was applied to the localization of aerodynamic noise on actual wind turbine blades. The resulting source distributions under different operating conditions were systematically analyzed and compared with existing experimental and numerical findings, further confirming the method's effectiveness in practical engineering settings. Nevertheless, several limitations remain for full-scale applications. First, the Doppler correction in the time domain depends on accurate estimation of the rotational Mach number; increased inflow turbulence may introduce additional correction errors. Second, the construction of the point spread function (PSF) is affected by array aperture and grid density, leading to significant computational burdens for large-scale arrays or utility-scale turbines.

Future work will focus on developing more efficient PSF modeling and solution strategies based on advanced sparse representations, enabling scalable and real-time aerodynamic noise localization for full-scale wind turbines.

Acknowledgement: Not applicable.

Funding Statement: This research was funded by the Natural Science Foundation of Inner Mongolia Autonomous Region (Grant No. 2024MS05063), the Special Project for First-Class Discipline Research (Grant No. YLXKZX-NGD-008), the Basic Research Operating Expenses Program for Colleges and Universities directly under the Inner Mongolia Autonomous Region (JY20220399), and the Research Start-up Fund Project of Inner Mongolia University of Technology (Grant No. BS2024022).

Author Contributions: The authors confirm contribution to the paper as follows: Conceptualization, Methodology, Writing—original draft, Writing—review and editing, Peng Wang; Conceptualization, Writing—original draft, Zhiying Gao; Writing—review and editing, Yongyan Chen; Formal analysis, Rina Su; Project administration, Supervision, Yefei Bai; Data curation, Jianlong Ma; Project administration, Investigation, Tianhao Zhang. All authors reviewed the results and approved the final version of the manuscript.

Availability of Data and Materials: Data available on request from the authors.

Ethics Approval: Not applicable.

Conflicts of Interest: The authors declare no conflicts of interest to report regarding the present study.

Nomenclature

$\boldsymbol{A}$	Point spread function
$\boldsymbol{A}_\gamma$	The point spread function at the corresponding position
A_γ^H	The conjugate transpose of the point spread function corresponding to the source location
c	Speed of sound, m/s
d	Index of the de-Doppler segment
D	Number of de-Doppler segments used for averaging
F_s	The sampling rate of the microphone, Hz
$\boldsymbol{G}(\omega)$	Frequency-domain Green's function matrix
L	Number of effective (active) sound sources
M	Total number of microphones
N	Number of monopole sound sources
$p(\boldsymbol{r}_m, t)$	Acoustic pressure, pa
$\hat{p}_m(\omega)$	Frequency-domain signal
$\boldsymbol{P}(\omega)$	Vector of microphone spectra
$Q_{i,j}$	The cross-correlation power
$\boldsymbol{Q}$	The true sound source power distribution
$Q_{nm}^{(d)}(\omega)$	Spectrum of the de-Doppler processed signal
$Q^{(d)}(\omega)$	Cross-spectral matrix of de-Doppler beamforming outputs
Q_Γ	Vector of contribution coefficients
$\boldsymbol{q}_\gamma$	Contribution coefficient of the source
$\boldsymbol{R}$	Cross-spectral matrix of microphone signals
$\boldsymbol{R}_\eta$	Cross-spectral matrix of array noise
$\boldsymbol{r}_m$	Spatial position vector of the microphone
$\boldsymbol{r}_n$	Position vector of the sound source
$\boldsymbol{r}_n(\tau)$	Instantaneous position vector of the rotating sound source

$\boldsymbol{S}(\omega)$	Frequency-domain matrix of the sound source
$s_n(t)$	Time-domain sound pressure signal
$\hat{s}_n(\omega)$	The frequency-domain signal
$\tilde{s}_{mn}(\tau)$	Time-domain de-Doppler reconstructed signal
$\tilde{s}_{nm}^{(d)}(\tau)$	De-Doppler processed time-domain signal
t	Reception time, s
$\boldsymbol{w}(\boldsymbol{r}_n, \omega)$	Steering vector
$\boldsymbol{v}(\tau)$	Tangential velocity vector
ω_n	Emission angular frequency, Hz
ω_m	Receiving angular frequency, Hz
$y(\boldsymbol{r}_n, \omega)$	Beamforming output
$Y_{n,n'}(\omega)$	Cross-correlation power, W
$\boldsymbol{Y}$	The observation result of the sound source map
$y_n^{(d)}(\omega)$	Averaged de-Doppler beamforming output
$\boldsymbol{\eta}(\omega)$	Vector of microphone self-noise spectra
$\hat{\eta}m(\omega)$	Frequency-domain self-noise of microphone
σ^2	Variance
$\boldsymbol{\Gamma}$	The index set of sparse sound source locations
γ	The index of a certain sound source location
τ	Emission time, s
$\mathcal{M}_{mn}(\tau)$	Mach number
Ω	Rotating speed, r/min
θ	Rotation Angle, °

Abbreviations

OMP	Orthogonal matching pursuit
DAMAS	The Deconvolution Approach for the Mapping of Acoustic Sources
TD	Time-domain De-doppler
CBF	Conventional beamforming
SVD	Singular Value Decomposition
ROSI	Rotating Source Identification
APM	The array matching method
TD-OMP-DAMAS	Time-Domain De-Depolarized Orthogonal Matching Pursuit Deconvolution Approach for the Mapping of Acoustic Sources
CLEAN-SC	CLEAN-Source Coherence

References

1. Zheng D, Yan X, Tong D, Davis SJ, Caldeira K, Lin Y, et al. Strategies for climate-resilient global wind and solar power systems. Nature. 2025;643(8074):1263–70. doi:10.1038/s41586-025-09266-7.
2. Yu H, Li Z, Guo Q, Qi L, Li N, Zhu K, et al. Experimental study of tower noise on the basis of blade-tower interaction. Front Energy Res. 2024;12:1449817. doi:10.3389/fenrg.2024.1449817.
3. Sun B, Cui H, Li Z, Fan T, Li Y, Luo L, et al. Experimental study on the noise evolution of a horizontal axis icing wind turbine based on a small microphone array. Sustainability. 2022;14(22):15217. doi:10.3390/su142215217.
4. Xue W, Yang B. Aeroacoustic source localization using the microphone array method with application to wind turbine noise. Int J Aeroacoust. 2024;23(5–6):533–57. doi:10.1177/1475472X241259122.
5. Yardibi T, Li J, Stoica P, Cattafesta LN. Sparsity constrained deconvolution approaches for acoustic source mapping. J Acoust Soc Am. 2008;123(5):2631–42. doi:10.1121/1.2896754.
6. Ramachandran RC, Raman G, Dougherty RP. Wind turbine noise measurement using a compact microphone array with advanced deconvolution algorithms. J Sound Vib. 2014;333(14):3058–80. doi:10.1016/j.jsv.2014.02.034.

7. Ocker C, Czwielong F, Chaitanya P, Pannert W, Becker S. Aerodynamic and aeroacoustic properties of axial fan blades with slitted leading edges. Acta Acustica. 2022;6:48. doi:10.1051/aacus/2022043.
8. Prospathopoulos JM, Voutsinas SG. Application of a ray theory model to the prediction of noise emissions from isolated wind turbines. Wind Energy. 2006;9(1–2):55–69. doi:10.1002/we.182.
9. Chu Z, Yang Y. Comparison of deconvolution methods for the visualization of acoustic sources based on cross-spectral imaging function beamforming. Mech Syst Signal Process. 2014;48(1–2):404–22. doi:10.1016/j.ymssp.2014.03.012.
10. Arcondoulis EJG, Liu Y, Xu P, Li Q, Wei R, Yang Y, et al. Experimentally based CLEAN-SC array pairing method for distributed aeroacoustic sources. Aiaa J. 2022;60(4):2678–84. doi:10.2514/1.J061270.
11. Padois T, Berry A. Orthogonal matching pursuit applied to the deconvolution approach for the mapping of acoustic sources inverse problem. J Acoust Soc Am. 2015;138(6):3678–85. doi:10.1121/1.4937609.
12. Sarradj E. Three-dimensional acoustic source mapping with different beamforming steering vector formulations. Adv Acoust Vib. 2012;2012:292695. doi:10.1155/2012/292695.
13. Ning F, Zhang C, Pan F, Liu Y, Wei J. Compressive sensing algorithm for sound source location of aircraft landing gear. Acta Aeronaut Astronaut Sin. 2018;39(5):121810. doi:10.7527/S1000-6893.2018.21810.
14. Pannert W, Maier C. Rotating beamforming—motion-compensation in the frequency domain and application of high-resolution beamforming algorithms. J Sound Vib. 2014;333(7):1899–912. doi:10.1016/j.jsv.2013.11.031.
15. Sijtsma P, Oerlemans S, Holthusen H. Location of rotating sources by phased array measurements. In: Proceedings of the 7th AIAA/CEAS Aeroacoustics Conference and Exhibit: American Institute of Aeronautics and Astronautics; 2001 May 28–30; Maastricht, The Netherlands. p. 1–13.
16. Zhang H, Kocsis B, Horvath C. Segmented ROSI method: beamforming method for investigating turbomachinery noise sources along segmented trajectories. Noise Control Eng J. 2022;70(1):62–76. doi:10.3397/1/37705.
17. Ye J, Li Y. Application of ROSI + CLEAN-SC algorithm on the measurement of rotating blade noise and its control. Appl Acoust. 2025;240:110866. doi:10.1016/j.apacoust.2025.110866.
18. Geng L, Ma J, Zhang X, Zhu S. A multistep time-domain plane wave superposition method for stabilizing the reconstruction of the non-stationary sound field. Mech Syst Signal Process. 2019;121:913–28. doi:10.1016/j.ymssp.2018.11.054.
19. Carillo K, Pires L, Padois T, Brailovski V, Doutres O. Enhancing low-frequency transmission loss in aircraft fuselage sidewalls with a flat array of covered Helmholtz resonators metamaterial. Aerosp Sci Technol. 2025;166:110571. doi:10.1016/j.ast.2025.110571.
20. Li W, Zhou C, Zhao S, Qin Y, Zhang R, Tang Y. Improved penalized beamforming using Hilbert curves for sound source identification with a microphone array. Meas Sci Technol. 2025;36(5):17. doi:10.1088/1361-6501/add311.
21. Brooks TF, Humphreys WM. A deconvolution approach for the mapping of acoustic sources using a microphone array. In: Proceedings of the 10th AIAA/CEAS Aeroacoustics Conference; 2004 May 10–12; Manchester, UK. p. 2004–954. doi:10.2514/6.2004-2954.
22. Roger M, Moreau S. Broadband self-noise from unsteady flow over airfoils. Annu Rev Fluid Mech. 2010;42(1):377–406. doi:10.1146/annurev-fluid-121108-145618.
23. Dougherty RP. Extensions of DAMAS and benefits and limitations of deconvolution in beamforming. In: Proceedings of the 11th AIAA/CEAS Aeroacoustics Conference; 2005 May 23–25; Monterey, CA, USA. p. 2005–961. doi:10.2514/6.2005-2961.
24. Sijtsma P. CLEAN based on spatial source coherence. Int J Aeroacoust. 2007;6(4):357–74. doi:10.1260/147547207783359459.
25. Tropp JA, Gilbert AC. Signal recovery from random measurements via orthogonal matching pursuit. IEEE Trans Inf Theory. 2007;53(12):4655–66. doi:10.1109/TIT.2007.909108.
26. Rodriguez S, Rebillat M, Paunikar S, Margerit P, Monteiro E, Chinesta F, et al. Single atom convolutional matching pursuit: theoretical framework and application to Lamb waves based structural health monitoring. Signal Process. 2025;231:109898. doi:10.1016/j.sigpro.2025.109898.
27. Gao K, Pan J, Jiang W. Identification of broadband sound sources rotating in the cylindrical duct with out-duct nonuniform measurements. Measurement. 2026;257(Part C):118721. doi:10.1016/j.measurement.2025.118721.

28. Chu N, Huang Q, Yu L, Ning Y, Wu D. Rotating acoustic source localization: a power propagation forward model and its high-resolution inverse methods. Measurement. 2021;174:109006. doi:10.1016/j.measurement.2021.109006.
29. Brooks T, Humphreys W. Effect of directional array size on the measurement of airframe noise components. In: Proceedings of the Fifth AIAA/CEAS Aeroacoustics Conference; 1999 May 10–12; Bellevue, WA, USA. Reston, VA, USA: American Institute of Aeronautics and Astronautics; 1999.
30. Lyu M, Yu L, Wang R, Fang Y. Deconvolution of acoustic beamforming maps in interference environments with mean-reverting stochastic differential equations. Mech Syst Signal Pr. 2025;237:113091. doi:10.1016/j.ymssp.2025.113091.
31. Yu L, Jing Q, Wang R, Ji R, Jiang W. Comparison of two state-of-the-art rotating dipole sound source imaging technologies: models, algorithms and applications. Appl Acoust. 2023;211:109515. doi:10.1016/j.apacoust.2023.109515.
32. Su R, Gao Z, Chen Y, Zhang C, Wang J. Large-eddy simulation of the influence of hairpin vortex on pressure coefficient of an operating horizontal axis wind turbine. Energy Convers Manag. 2022;267:115864. doi:10.1016/j.enconman.2022.115864.
33. Liu W, Qiang X, Shang D, Qin Q, Liu L, Liu Y. Effects of wall heating on wall pressure fluctuations and flow noise in a low-Reynolds-number turbulent channel flow with temperature-dependent viscosity. Phys Scripta. 2024;99(11):24. doi:10.1088/1402-4896/ad8401.
34. Zhang CQ, Gao ZY, Chen YY, Dai YJ, Wang JW, Zhang PW. Experimental determination of the dominant noise mechanism of rotating rotors using hot-wire anemometer. Appl Acoust. 2021;173:107703. doi:10.1016/j.apacoust.2020.107703.
35. Oerlemans S, Sijtsma P, Lopez BM. Location and quantification of noise sources on a wind turbine. J Sound Vib. 2007;299(4–5):869–83. doi:10.1016/j.jsv.2006.07.032.
36. Su R, Gao Z, Chen Y, Bai Y, Wang J. Experimental on the fatigue failure areas of wind turbine blades' rotating fundamental frequency. AIP Adv. 2023;13(6):14. doi:10.1063/5.0142967.
37. Manganelli F, Bernardi C, Giannotta A, Leonardi S, Cherubini S, De Palma P. The effect of Coriolis force on the coherent structures in the wake of a 5MW wind turbine. Energy Convers Manag X. 2025;25(1):100830. doi:10.1016/j.ecmx.2024.100830.